









Article

1,10-Phenanthroline-Iron Complex-Derived Fe-N-C Electrocatalysts: Enhanced Oxygen Reduction Activity and Stability Through Synthesis Tuning

Carlos S. A. Vasconcellos ¹ , Nelson A. Galiote ¹ , Nadeem Khan ¹ , Enrique A. Paredes-Salazar ¹ , Maykon L. Souza ¹ , Kotaro Sasaki ² , Meng Li ³  and Fabio H. B. Lima ^{1,*} 

¹ São Carlos Institute of Chemistry, University of São Paulo, Av. Trabalhador São-Carlense 400, São Carlos 13566-590, SP, Brazil

² Chemistry Division, Brookhaven National Laboratory, Upton, NY 11973, USA

³ Center for Functional Nanomaterials, Brookhaven National Laboratory, Upton, NY 11973, USA

* Correspondence: fabiohbl@iqsc.usp.br

Abstract

The development of electrocatalysts composed of earth-abundant elements is essential for advancing the commercial application of Proton Exchange Membrane Fuel Cells (PEMFC). Among these, single-atom electrocatalysts, such as Fe-N-C, show great promise for the oxygen reduction reaction (ORR). This study aims to improve the ORR activity and stability of Fe-N-C electrocatalysts by fine-tuning the straightforward 1,10-phenanthroline-iron complexation synthesis method. Key parameters, including iron-to-phenanthroline ratio, carbon powder surface area, and pyrolysis temperature were systematically varied to evaluate their influence on the resulting electrocatalysts. The findings of this study revealed that the electrocatalysts synthesized with 1,10-phenanthroline (Phen) and high-surface-area Black Pearls (BP) possessed much better ORR activity than electrocatalysts prepared by using Vulcan carbon (lower surface area). Interestingly, electrocatalysts prepared with BP, but with a non-bidentate nitrogen-containing ligand molecule, such as imidazole, showed a much poorer activity, as the resulting material predominantly consisted of inactive structures, such as encapsulated iron nanoparticles and iron oxide, as evidenced by HR-TEM, EXAFS, and XRD. Therefore, the results suggest that only the synergistic combination of the bidentate ligand phenanthroline (Phen) and the high-surface-area carbon support (BP) favored the formation of ORR-active Fe-N-C single-atom species upon pyrolysis. The study also unveiled a significant enhancement in electrocatalyst stability during accelerated durability tests (and air storage) as the pyrolysis temperature was increased from 700 to 1300 °C, albeit at the expense of ORR activity, likely resulting from the generation of iron particles. Pyrolysis at 1050 °C yielded the electrocatalyst with the most favorable balance of activity and stability in rotating disk measurements, while maintaining moderate durability under PEM fuel cell operation. The insights obtained in this study may guide the development of more active efficient and durable electrocatalysts, synthesized via a simple method using earth-abundant elements, for application in PEMFC cathodes.

Keywords: oxygen reduction; Fe-N-C; single-atom; PEM fuel cell cathode; earth-abundant electrocatalysts



Academic Editor: Hao Xu

Received: 26 June 2025

Revised: 21 August 2025

Accepted: 26 August 2025

Published: 29 August 2025

Citation: Vasconcellos, C.S.A.; Galiote, N.A.; Khan, N.; Paredes-Salazar, E.A.; Souza, M.L.; Sasaki, K.; Li, M.; Lima, F.H.B. 1,10-Phenanthroline-Iron Complex-Derived Fe-N-C Electrocatalysts: Enhanced Oxygen Reduction Activity and Stability Through Synthesis Tuning. *Catalysts* **2025**, *15*, 821. <https://doi.org/10.3390/catal15090821>

Copyright: © 2025 by the authors. Licensee MDPI, Basel, Switzerland. This article is an open access article distributed under the terms and conditions of the Creative Commons Attribution (CC BY) license (<https://creativecommons.org/licenses/by/4.0/>).

1. Introduction

Hydrogen-powered proton exchange membrane fuel cells have so far demonstrated potential viability for vehicles and stationary applications [1]. For the cathode, the state-of-the-art platinum and other noble metal-based electrocatalysts have been globally tested and admired as promising candidates to catalyze the sluggish kinetics of the oxygen reduction reaction (ORR). Up to now, the most frequently employed electrocatalysts are alloys and nanoparticles of Pt or Pd, supported on high-surface-area carbon powders [2]. From the perspective of computational calculations acquired through density functional theory (DFT), these noble metals have so far occupied the peaks of electrocatalyst volcano plots, owing to their potentially high catalytic activities. However, the scarcity and exorbitant prices of platinum and its counterparts have hampered its validity appeal over a broad spectrum of applications, mass production, and commercialization of fuel cells. Thus, it is likely to either reduce or eliminate the use of platinum and other noble metals to make PEMFCs cost-competitive with respect to conventional technologies (for instance, batteries and internal combustion engines). Therefore, the scientific community worldwide is striving to explore novel low cost and easily accessible alternatives for platinum and other noble metal-based catalysts in fuel cells for automotives.

Two types of technological approaches have been paved to cope with the challenge of highly priced platinum-group metals (PGM) electrocatalysts. In this regard, one way is to introduce low loading PGM catalysts (with low dosage of noble metals), and another way is to launch an alternative or platinum-group metal-free catalysts (PGM-free), by inculcating the employment of earth-abundant metals such as Fe, Cu, Co, and Mn [3]. Significant developments have bestowed the hope for acquiring the “holy grail” of incorporating low-priced metals like Fe and Co to PEMFCs [4]. However, it is woeful to mention that, nevertheless, Fe and Co-based PEMFCs are more vulnerable to a conundrum of stability and performance issues, especially in harsh acidic and oxygen (or air)-containing atmosphere protocol of the proton membrane fuel cells, which severely provokes the devastation of the catalyst. Recently, these stability and catalytic performance concerns associated with use of PEMFCs have persuaded researchers globally to explore deep insights into their stability, durability, and activity issues [5,6]. The main degradation mechanisms include peroxide and radical attack (formation of hydrogen peroxide and reactive oxygen species, leading to corrosion of carbon and active Fe-N-C sites) [7–9], which is more severe in acid than in alkaline [10]; electrochemical carbon corrosion (high potentials experienced by the cathode during fuel cell shutdown or start-up); demetallation (leaching of Fe ions, reducing the density of active sites) due to iron corrosion [11,12]; protonation (the acidic PEM condition may lead to the protonation of the nitrogen atom, decreasing the electrocatalyst turn over frequency and/or weakening the metal–nitrogen coordination and diminishing ORR activity) [13]; and micropores flooding (hampers the accessibility of oxygen to Fe-N_x sites thereby declining the performance of the fuel cell [14]. Attempts to enhance the electrocatalytic activity of Fe-N-C ORR electrocatalysts are also under focus. Researchers have explored a range of strategies, such as increased Fe-N coordination (optimizing pyrolysis conditions and precursor ratios); single-atom dispersion (involving techniques like atomic layer deposition [15,16], and the use of chelating agents, e.g., phenanthroline); dual-metal doping (incorporating secondary metals) alongside iron [17] and number of iron atoms [18], which can synergistically enhance the electronic structure, ORR kinetics, and structural and morphological control (Porous Carbon Frameworks, and/or 3D Carbon Architectures); electronic structure tuning (heteroatom doping); and synthesis optimization (controlled or multi-step pyrolysis or post-pyrolysis treatments) [19,20].

The single-atom dispersion can involve the use of chelating agents, such as phenanthroline [21–23]. The use of Phen as a nitrogen-rich organic ligand in the synthesis of

Fe-N-C catalysts has emerged as an effective strategy for generating high-performance electrocatalysts for the oxygen reduction reaction (ORR) [16]. Phenanthroline is a heteroaromatic compound containing two nitrogen atoms with strong chelating ability, which ensures the formation of stable Fe-N coordination complexes. This approach enables precise control over the incorporation of Fe-N sites and, thus, enhances the distribution of active sites in the carbon matrix. M. Kim et al. [22] reported the study of phenanthroline isomers used as precursors to reveal the correlation between precursor coordination and ORR activity of Fe-N-C electrocatalysts. The results showed that the preferential formation of Fe-N_x active sites was achieved only with 1,10-phenanthroline (higher degree of Fe-N coordination; bidentate), featuring homogeneously distributed Fe single-atoms, and highly retained pyridinic N [24–26]. This result evidenced the role of the precursors with multiple coordination for the effective derivation of Fe-N_x active sites for the ORR. Considering that the phenanthroline-complexation method for preparing Fe-N-C electrocatalysts is relatively simple, and that studies focused on its optimization as well as on activity and durability tests in half-cells and PEM fuel cells remain scarce, the present work is devoted to a systematic investigation of synthesis parameters, including the effect of pyrolysis temperature on the electrocatalyst activity and stability, both during operation and storage. The goal is to enhance the electrocatalytic performance and operational stability of Fe-N-C, thereby advancing the development of precious-metal-free electrocatalysts for PEM fuel cells.

2. Results and Discussion

2.1. Characterization

The first attempt of this study was related to the study of the effect of relative nitrogen and iron content on the resulting Fe-N-C material. The nominal iron-to-nitrogen atomic ratio was changed from 1:4 to 1:27, by varying the initial relative weight of the components for the complexation step during the synthesis, as presented in Table S1, and the pyrolysis was set at 1050 °C, in Argon atmosphere [27]. Here, it is worth mentioning that increasing the nitrogen content beyond 1:27 was not experimentally feasible, as the resulting impregnated carbon material exhibited a vitreous appearance rather than a powdered form. Therefore, the maximum attainable Fe-to-N ratio was limited to 1:27, which already exceeds the stoichiometric requirement of the [Fe(Phen)₃]²⁺ complex (see Experimental Section). As shown in the X-ray Diffraction (XRD) patterns in Figure 1a, increasing the amount of phenanthroline leads to the gradual vanishing of the diffraction peak at approximately 36°, which is associated with iron oxide species (there are only the presence of two broad peaks related to the amorphous carbon powder). The complete suppression of the diffraction peak is observed exclusively upon the use of the highest phenanthroline loading. For lower amounts of Phen, it is likely that the “lack” of N-containing molecules (Phen) leads to a low number of N-doped carbon sites for the proper Fe anchoring during the pyrolysis step and, so, it may allow the agglomeration of iron [28]. The progressive disappearance of particulate structures with increasing phenanthroline content is further corroborated by Transmission Electron Microscopy (TEM) analysis (Figure S1), which shows an absence of detectable particles at an Fe-to-N ratio of 1:27. (When all synthesis parameters are held constant and the iron loading is increased to 5 or 10 wt.%, additional diffraction peaks emerge, corresponding to the formation of metallic iron, iron carbide, and iron nitride phases, as shown in Figure S2). This indicates a loss of efficiency in achieving atomic iron dispersion at higher Fe loadings).

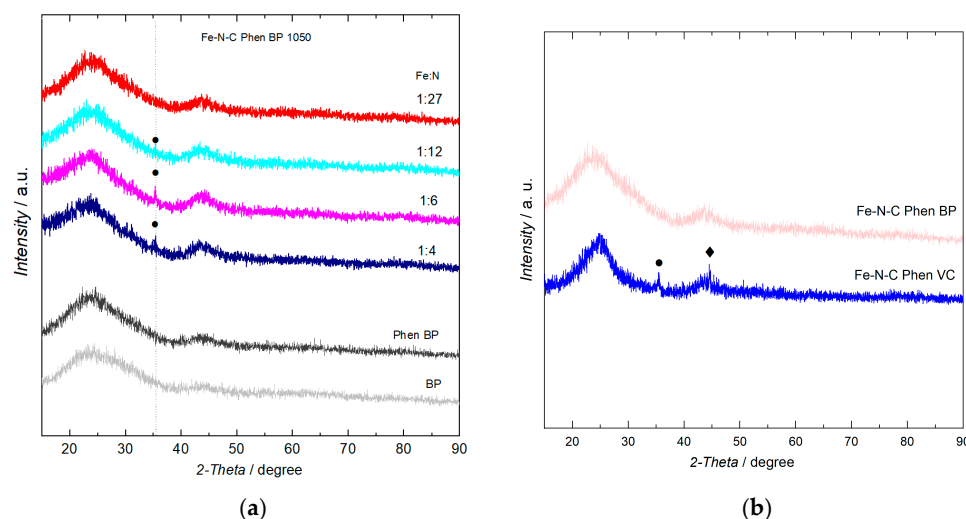


Figure 1. X-ray powder diffraction for the Fe-N-C Phen BP electrocatalysts synthesized with different iron-to-nitrogen ratios (a) and X-ray powder diffraction for the Fe-N-C electrocatalysts synthesized using Phen and Vulcan carbon (blue) or Black Pearls (red) (b). The symbols indicated the presence of iron oxide (circle) and metallic iron (rhombus) species.

Notably, when imidazole was employed as the nitrogen precursor under the same synthesis conditions and maintaining an Fe-to-N ratio of 1:27, XRD analysis revealed the presence of crystalline iron oxide phases, rather than the formation of atomically dispersed iron species (Figure S3). These findings underscore that, beyond the requirement for nitrogen in excess to achieve effective carbon doping, strong coordination between the iron center and the ligand is essential to stabilize isolated Fe-N-C sites and suppress the aggregation into less active iron-containing phases. Interestingly, when the synthesis was performed using the optimized phenanthroline content, corresponding to the maximum Fe-to-N ratio of 1:27, but employing Vulcan carbon (Fe-N-C Phen VC) instead of BP, the resulting material exhibited features similarly to those obtained with lower phenanthroline loadings on BP (Figure 1b).

Further analyses were carried out via X-ray Absorption Spectroscopy (XAS). The Fourier Transform (FT) of the Extended X-ray Absorption Fine Structure (EXAFS) oscillations, at the Fe K edge, for electrocatalysts synthesized with Phen (in excess, i.e., 1:27) and Vulcan or Black Pearls carbon powder is shown in Figure 2a. The reference spectra for iron oxide, iron nitrate, and metallic iron were included for comparison. For Fe-N-C Phen VC, one can note a peak at around 1.5 Å, indicating Fe-N coordination, but with one additional peak at about 2.8 Å, which reveals the Fe-O-Fe coordination, implying the presence of iron oxide particles, in corroboration with the XRD result [29]. On the other hand, for Fe-N-C Phen BP, it is only observed a peak around 1.5 Å, suggesting the Fe-N coordination [23,30]. Figure 2b displays the STEM results with elemental mapping for the Fe-N-C Phen BP and Fe-N-C Phen VC samples. The elemental maps clearly show that the Fe-N-C Phen BP electrocatalyst exhibits a highly homogeneous dispersion of iron and nitrogen on the carbon matrix. Conversely, the images for Fe-N-C Phen VC display distinct agglomerates composed of iron and oxygen, indicative of iron oxide formation, which aligns well with the observations from XRD and EXAFS measurements (additional images with the mapping for iron, nitrogen, oxygen, and carbon are presented in Figure S4). The presence of iron oxide particles was further validated by Scanning Transmission Electron Microscopy measurements (STEM) coupled with elemental mapping and High-resolution Transmission Electron Microscopy (HR-TEM) analyses, as shown in Figure S5A,B. The HR-TEM image in Figure S5B clearly reveals crystalline domains consistent with iron oxide, as evidenced by the lattice fringes and corroborated by the corresponding elemental

mapping presented alongside. As shown in Table S2, the surface area of pyrolyzed pure BP and VC carbons is $1700 \text{ m}^2 \text{ g}^{-1}$ and $230 \text{ m}^2 \text{ g}^{-1}$, respectively. The corresponding Fe-N-C materials, synthesized with Phen, Fe-N-C Phen BP, and Fe-N-C Phen VC, exhibit surface areas of $840 \text{ m}^2 \text{ g}^{-1}$ and $255 \text{ m}^2 \text{ g}^{-1}$, respectively, thus reflecting the trend imposed by the surface area of the carbon precursors. Given that the high-surface-area BP carbon was required to achieve atomic dispersion, it can be concluded that the carbon support plays a pivotal role in suppressing iron aggregation. Furthermore, in addition to the necessity of nitrogen excess for effective carbon doping, strong iron chelation by the nitrogen precursor is also essential to favor the formation of atomically dispersed and catalytically active Fe-N-C sites.

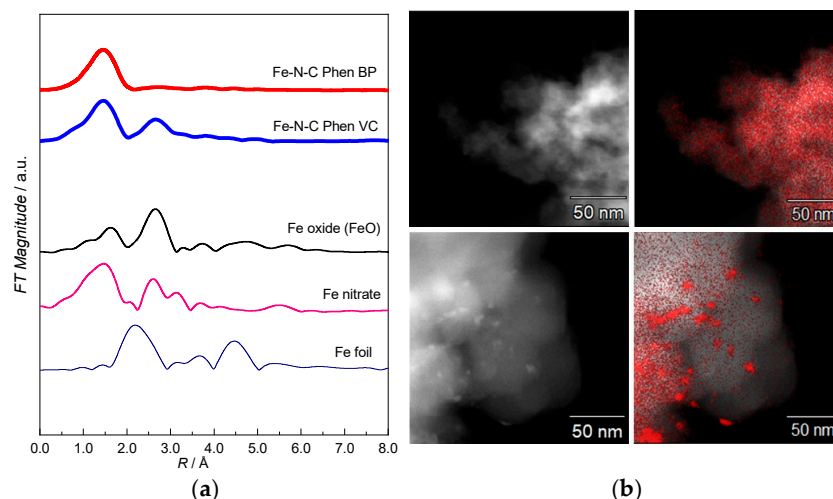


Figure 2. (a) Fourier Transform of the EXAFS oscillations, K^3 -weighted, at the Fe (7112 eV) K edge, for the Fe-N-C electrocatalysts synthesized with phenanthroline and Vulcan carbon (blue) or phenanthroline and Black Pearls (red). The reference spectra for iron oxide (FeO) and iron nitrate were included for comparison; (b) STEM images and the corresponding elemental mapping for iron (red) for the Fe-N-C electrocatalysts synthesized using phenanthroline and Black Pearls (top) or Vulcan carbon (bottom).

For the electrocatalyst synthesized with a high phenanthroline loading (Fe-to-N ratio of 1:27), no diffraction peaks were observed by XRD, and elemental mapping revealed no signs of iron agglomeration. To further investigate the structural nature of the iron species, additional characterization was carried out using HR-TEM and Aberration-corrected High-angle Annular Dark Field Scanning Transmission Electron Microscopy (AC HAADF-STEM). As shown in Figure 3a–d, both HR-TEM and AC HAADF-STEM images confirm the absence of iron-containing nanoparticles or aggregates, strongly suggesting the formation of atomically dispersed Fe-N-C species. In particular, Figure 3d displays isolated bright spots uniformly distributed over the carbon matrix, which are consistent with individual iron atoms coordinated in Fe-N-C moieties, known to be active for the oxygen reduction [22]. The Fe content of the Fe-N-C Phen BP (1050 °C, 1:27) electrocatalyst was determined by acid digestion followed by Inductively Coupled Plasma Mass Spectrometry (ICP-MS) analysis, yielding 1.1 wt.% Fe. Combining this bulk composition with the electrode loading (which is utilized in the electrochemical experiments of the next section; 0.6 mg cm^{-2}) results in an RDE iron loading of approximately $6.0 \text{ } \mu\text{g Fe cm}^{-2}$. The literature reports typical Fe-N-C ink loadings in the range of $200\text{--}400 \text{ } \mu\text{g cat cm}^{-2}$. For instance, a loading of $200 \text{ } \mu\text{g cm}^{-2}$ with 1.0 wt.% Fe yields $2.0 \text{ } \mu\text{g Fe cm}^{-2}$, which is representative of typical RDE loadings for Fe-N-C catalysts ($200 \text{ } \mu\text{g cm}^{-2}$). X-ray photoelectron spectroscopy (XPS) analysis performed on the Fe-N-C Phen BP sample revealed the characteristic signals of iron and nitrogen (Figure S6). Notably, the absence of the peak at $\sim 706.7 \text{ eV}$ indicates the

nonexistence of iron metallic nanoparticles or aggregates, in agreement with the HR-TEM, STEM, and XAS results. The results evidence the presence of pyridinic and graphitic nitrogen species, both of which are recognized for their crucial contribution to the oxygen reduction activity of the electrocatalyst. Curiously, for high-temperature ORR systems, such as those employed in Solid Oxide Fuel Cells (SOFCs), it is the presence of oxygen species and/or oxygen vacancies, rather than nitrogen, that plays a dominant role in determining catalytic performance, as previously demonstrated [31]. In summary, the results demonstrate that the formation of ORR-active Fe-N-C single-atom species during pyrolysis is enabled exclusively by the synergistic interplay between the bidentate ligand and the high-surface-area carbon support.

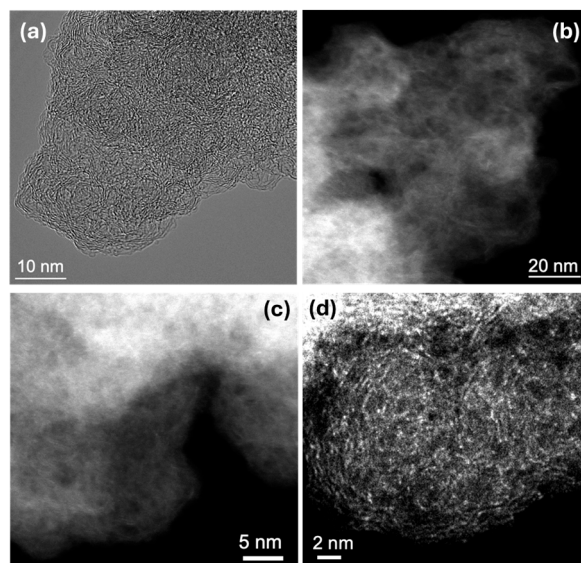


Figure 3. HR-TEM (a), STEM with different magnifications (b,c), and Aberration-corrected HAADF-STEM images of the Fe-N-C electrocatalyst synthesized with Phen and BP carbon (1050 °C 1:27); the bright spots in (d) show the iron single-atom species.

2.2. Electrochemical Results

The obtained linear sweep voltammetry (LSV) curves for the ORR on the electrocatalysts synthesized with different iron-to-phenanthroline ratios are shown in Figure 4a. One can observe a progressive increase in the half-wave potential as the Phen load is increased, indicating an increase in the ORR activity as more single-atom moieties are formed. Increasing the iron loading in the electrocatalysts to 5 and 10 wt.% resulted in a marked decrease in the half-wave potential in the LSV curves (Figure S7), attributed to the formation of ORR-inactive iron particles during pyrolysis (Figure S2). Interestingly, when imidazole (Imi) was used as the nitrogen precursor instead of Phen, the resulting electrocatalyst exhibited significantly lower ORR activity (Figure S8). These results clearly demonstrate that imidazole fails to promote the formation of catalytically active Fe-N-C sites, with XRD analysis revealing the presence of an ORR-inactive metallic iron phase (Figure S3), in sharp contrast to the outcomes obtained with phenanthroline. Figure 4b presents the LSV curves for the ORR on the synthesized Fe-N-C Phen VC and Fe-N-C Phen BP electrocatalysts, revealing a markedly higher half-wave potential for the material prepared using Black Pearls carbon. Complementary, cyclic voltammetry (CV) measurements (Figure S9) show significantly higher pseudocapacitive currents for the BP-based electrocatalyst, consistent with its substantially higher surface area (Table S2). Collectively, these results indicate that the inferior ORR activity of the Vulcan carbon-derived electrocatalyst arises from its lower

surface area, which limits the extent of Fe-N-C site formation by hindering iron dispersion and favoring the formation of iron particles.

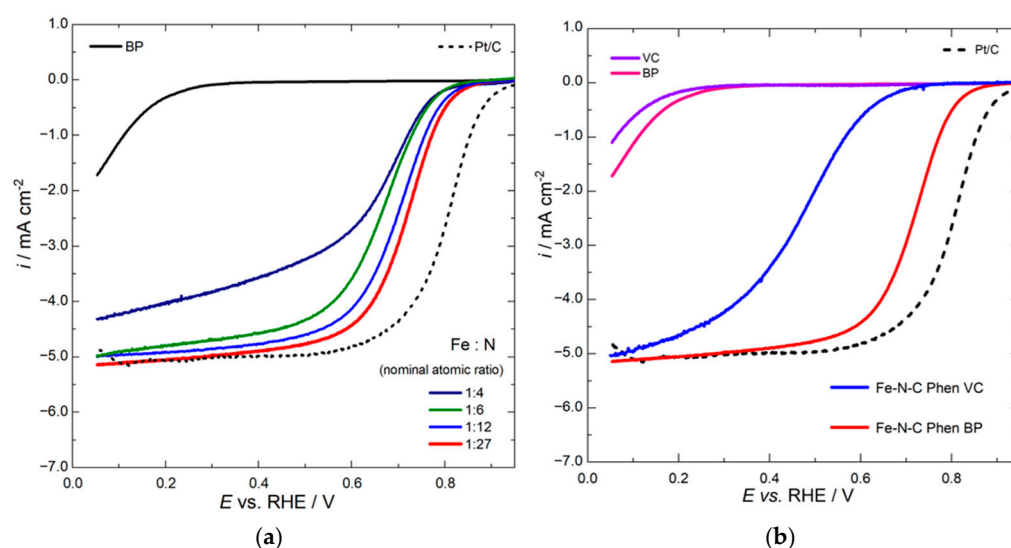


Figure 4. Linear sweep voltammetry curves for the oxygen reduction on Fe-N-C electrocatalysts synthesized using phenanthroline and Black Pearls carbon, with different iron-to-nitrogen ratios (a), and synthesized using phenanthroline and Black Pearls or Vulcan carbon (b), obtained in O₂-saturated 0.5 mol L^{−1} H₂SO₄ electrolyte, with scan rate of 1.0 mV s^{−1} and rotation rate of 1600 rpm.

As an attempt to enhance the ORR activity of the Vulcan-derived material, the sample was subjected to an additional pyrolysis step in an NH₃ atmosphere at 900 °C. However, as shown in Figure S10, the ORR polarization curve displayed only a marginal positive shift in potential. EXAFS analysis (Figure S11) revealed that the NH₃ treatment promoted the conversion of iron oxide into metallic iron nanoparticles, which are inactive toward the ORR and unstable under acidic conditions due to dissolution. The slight activity enhancement may be attributed to the limited formation of Fe-N-C moieties upon NH₃ exposure, indicating that this treatment is not effective for extensive Fe-N-C site generation. These results further demonstrate that pre-existing iron particles cannot be fully converted into single-atom species under a reductive NH₃ atmosphere. Although pyrolysis under argon could, in principle, favor such conversion, the intrinsically low surface area of Vulcan carbon remains unfavorable for achieving high iron atomic dispersion.

D. Xia et al. [32] reported an effective strategy to significantly improve both catalytic and storage stability through high-temperature pyrolysis. In line with this approach, further synthesis optimization was carried out in the present study by investigating the effect of pyrolysis temperature on electrocatalyst activity and stability, while maintaining all other parameters at their optimized values (1.0 wt.% Fe and an Fe:N ratio of 1:27). The XRD patterns of electrocatalysts synthesized at pyrolysis temperatures ranging from 700 to 1300 °C are presented in Figure 5. When the temperature reaches 1200 °C, additional diffraction peaks assigned to iron carbide, metallic iron, and iron oxide become evident, indicating the agglomeration and phase transformation of iron species. As suggested in Ref. [32], this phenomenon is linked to nitrogen depletion at elevated temperatures, which disrupts Fe-N coordination and facilitates iron migration and structural rearrangement. In addition to XRD, Raman spectroscopy was performed on the Fe-N-C Phen BP samples pyrolyzed at different temperatures. As shown in Figure S12, the spectra display slight variations in the D' and D'' bands. The D' band (~1610–1620 cm^{−1}) originates from graphitic domains, whereas the D'' band (~1500–1550 cm^{−1}) is attributed to disordered amorphous carbon networks, or poor structural ordering. Notably, the D'/D'' intensity ratio increases

with pyrolysis temperature, reflecting an enhancement in the graphitic character of the carbon powder, consistent with earlier observations [32].

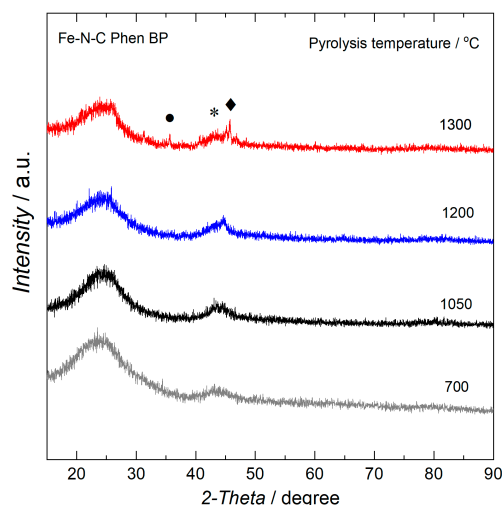


Figure 5. X-ray powder diffraction for the Fe-N-C electrocatalysts synthesized using Phen and Black Pearls carbon pyrolyzed at different temperatures. The symbols indicated the presence of iron oxide (circle), metallic iron (rhombus), and iron carbide (asterisk) species.

Figure 6 presents the ORR polarization curves for electrocatalysts prepared at different pyrolysis temperatures. The half-wave potentials for the samples synthesized at 700 °C and 1050 °C are essentially identical, indicating comparable activity. In contrast, catalysts obtained at higher pyrolysis temperatures (1200 and 1300 °C) exhibited a pronounced decrease in activity. It is worth noting that a synthesis at 500 °C was also performed; however, the resulting material showed poor ORR stability, with activity declining sharply after the first LSV cycle, and was therefore not further investigated. The reduced ORR performance observed for the samples prepared at 1200 and 1300 °C is likely associated with a lower density of Fe-N-C active sites, resulting from increased carbon graphitization and nitrogen loss during high-temperature pyrolysis, as previously reported [28,31].

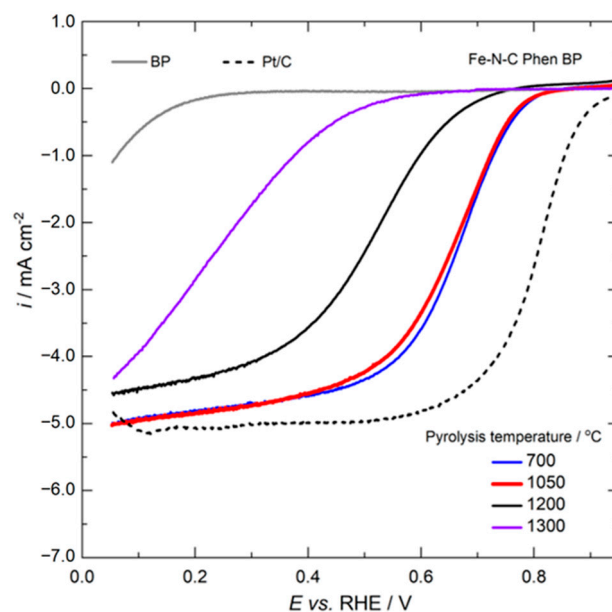


Figure 6. Linear sweep voltammetry curves for the oxygen reduction on Fe-N-C synthesized using Phen and BP, pyrolyzed at different temperatures, as indicated in the figure inset, obtained in O₂-saturated 0.5 mol L^{−1} H₂SO₄ electrolyte, with scan rate of 1.0 mV s^{−1} and rotation rate of 1600 rpm.

The shelf-life (storage in air) of most ORR-active electrocatalysts (synthesized at 700 and 1050 °C) was monitored. Their activities were assessed after storage in the laboratory, and the obtained polarization curves are shown in Figure S13. The results indicated a considerable decay in the activity for the material pyrolyzed at 700 °C, measured months after being synthesized. In contrast, for the material pyrolyzed at 1050 °C, the ORR curves were highly stable, even after 9 months under the same storage conditions. This indicates that stability during storage is strongly dependent on the pyrolysis temperature. Accelerated Stability Tests (AST) for the synthesized electrocatalysts were carried out, involving 10 k potential steps from 0.6 to 0.9 V vs. RHE, in O₂-saturated electrolyte, followed by linear voltammetry measurements for the ORR, at 1600 rpm. The obtained LSV for the ORR, after the AST, on Fe-N-C Phen BP, pyrolyzed at 700, 1050, 1200, and 1300 °C are presented in Figure 7. One can note expressive higher stability for the electrocatalyst pyrolyzed at 1200 and 1300 °C, but at the cost of lower ORR half-wave potential. The material prepared at 700 °C demonstrated high ORR activity but exhibited poor stability. Conversely, the electrocatalyst pyrolyzed at 1050 °C achieved the optimal balance between ORR activity and stability. The activity and stability of the best performing Fe-N-C electrocatalyst (optimal balance activity–stability) was also evaluated in a PEM fuel cell. The obtained polarization curve for the Fe-N-C Phen BP 1050-assembled PEM fuel cell, presented in Figure 8a, shows a peak power density of ca. 0.225 W cm^{−2}, which is relatively low when compared to high-active Fe-N-C electrocatalysts in the literature (ca. 0.6 W cm^{−2}) [32]. On the other hand, it maintained moderate durability under PEM fuel cell operation during 50 h.

The pyrolysis temperature, as noted, is a critical parameter that governs both the activity and durability of phenanthroline-iron complex-derived Fe-N-C electrocatalysts [33]. This parameter directly affects the degree of carbon graphitization, nitrogen retention, and the dispersion of iron species. At low pyrolysis temperatures (<700 °C), incomplete carbonization and low graphitization occur, resulting in high nitrogen retention but with unstable Fe-N-C moieties. The less ordered carbon matrix is more susceptible to oxidation and electrochemical corrosion under ORR conditions, which explains the poor storage stability and accelerated degradation observed during accelerated stress tests (AST). In the intermediate temperature range (~800–1050 °C), a balanced degree of carbon ordering and nitrogen retention favors the optimal formation of N-coordinated iron moieties (Fe-N₄) and promotes good dispersion of iron atoms. In this range, sufficient graphitization enhances corrosion resistance, while the Fe-N coordination is relatively well preserved, maintaining active site integrity over time. Consequently, at least for the synthesis method utilized herein, this interval represents the optimal compromise between activity and durability. At high pyrolysis temperatures (>1100 °C), the carbon matrix reaches a high degree of graphitization, but significant nitrogen loss occurs, leading to partial collapse of Fe-N coordination and increased mobility of Fe species. These conditions promote the aggregation of Fe into metallic nanoparticles or carbides (Figure 5), which are inactive toward the ORR. As a result, the ORR activity decreases despite the structural robustness of the carbon matrix. Interestingly, the stability of the electrocatalysts prepared at 1200 and 1300 °C is remarkable under potential cycling. In particular, the material prepared at 1200 °C, whose ORR half-wave potential remains relatively high, appears to be a promising candidate for future optimization strategies aimed at improving electrocatalytic activity without compromising its inherent stability.

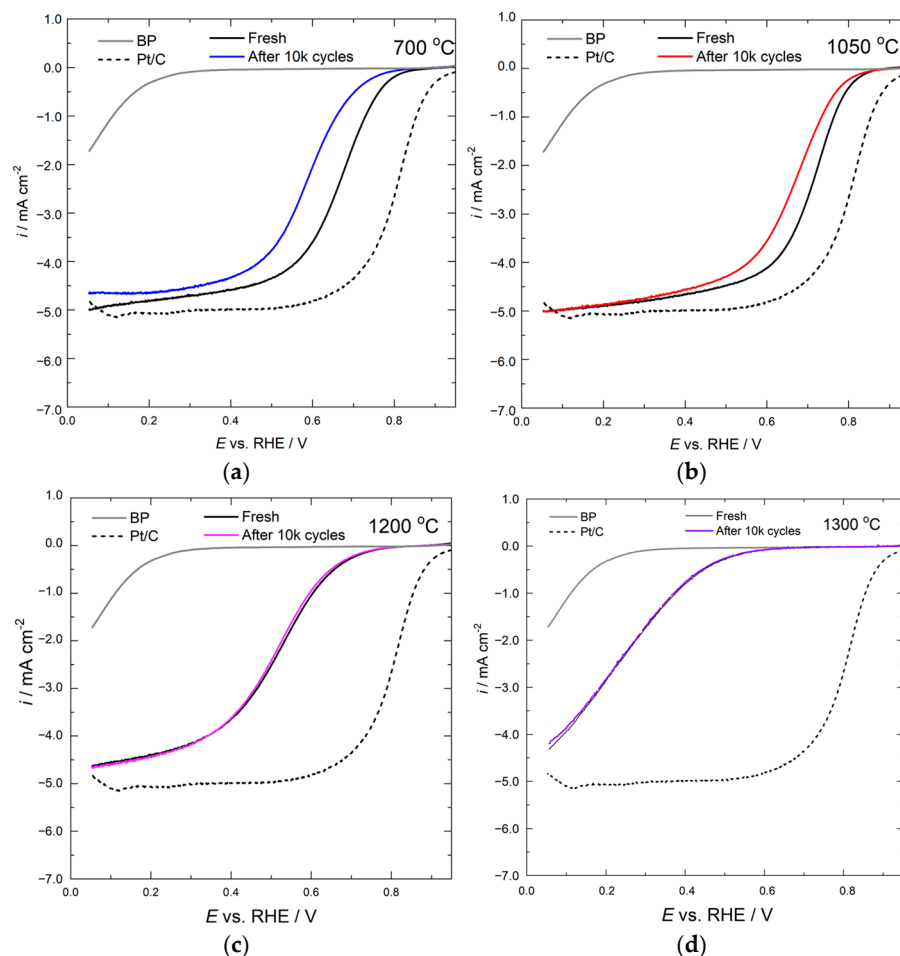


Figure 7. Linear sweep voltammetry curves recorded before and after 10 k cycles during the AST protocol for the electrocatalysts synthesized at pyrolysis temperatures of 700 °C (a), 1050 °C (b), 1200 °C (c), and 1300 °C (d), obtained in O_2 -saturated 0.5 mol L $^{-1}$ H_2SO_4 electrolyte, with scan rate of 1.0 mV s $^{-1}$ and rotation rate of 1600 rpm.

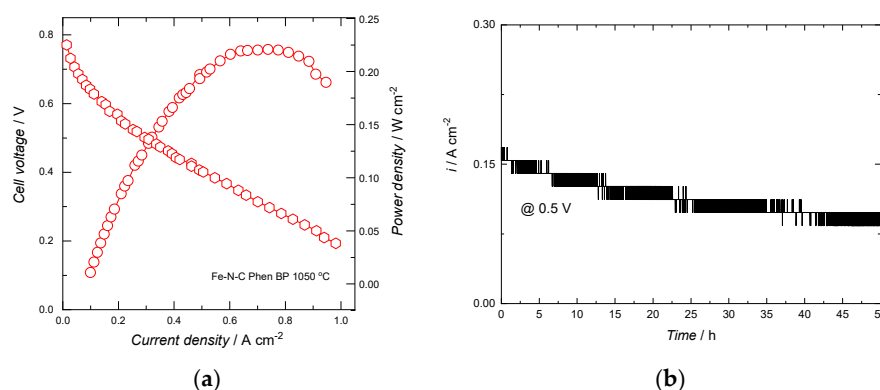


Figure 8. Activity and stability performance measurements of the Fe-N-C Phen BP 1050 electrocatalyst in PEMFCs: (a) polarization plots and corresponding current density–power density curves in H_2/O_2 PEMFCs. Testing conditions: H_2/O_2 flow of 200 mL min $^{-1}$ H_2/O_2 partial pressure of 2.0 bar, H_2/O_2 relative humidity of 100%, anode catalyst loading of 0.4 mg $_{Pt}$ cm $^{-2}$, cathode catalyst loading of 4.0 mg $_{FeNC}$ cm $^{-2}$; (b) chronoamperometry curve @ 0.5 V at the same conditions.

The focus of this manuscript was the optimization of the synthesis condition (bidentate ligand, phenanthroline versus mono or nonligand, imidazole; iron content; carbon powder surface area: Black Pearls versus Vulcan carbon; and pyrolysis temperature). As 1,10-phenanthroline has a relatively high cost, this limits large-scale availability and, thus,

it can hinder its use in commercial production of Fe-N-C catalysts for PEM fuel cells. Hence, the use of cheaper and more abundant ligands could reduce production costs while maintaining effective control over Fe coordination. As a cost-effective replacement strategy, hybrid approaches may be considered combining a strong chelating ligand (e.g., bipyridine) in small quantities with a bulk nitrogen source (such as melamine plus a small fraction of the ligand) to reduce the ligand usage while preserving high Fe dispersion. Additionally, biomass-derived nitrogen ligands [34], such as agricultural residues rich in amino or heterocyclic compounds, could serve as sustainable precursors.

3. Experimental

3.1. Synthesis of Electrocatalysts

The electrocatalysts employed in this work with nomenclature Fe-N-C iron-based single atom catalysts were synthesized using impregnation/complexation of nitrogen, carbon, and iron precursors and with subsequent high temperature pyrolysis [21]. Precursors comprising appreciable amounts of carbon, nitrogen, and iron were taken in desired quantities to synthesize structures with coordination and forthcoming fabrication of iron based single-atom catalyst. In this regard iron (III) nitrate nonahydrate ($\text{Fe}(\text{NO}_3)_3 \cdot 9\text{H}_2\text{O}$) was the iron precursor, while phenanthroline (and, in some cases, imidazole, depending on the experiment) was the nitrogen (and carbon) precursor, being impregnated in carbon powder: Black Pearls (BP, Cabot Corporation, Boston, MA, USA, 2000) or Vulcan carbon (VC, XC-72R). The electrocatalysts were synthesized by impregnation via refluxing in ethanol as solvent, with subsequent drying, and ultimately high-temperature treatment of powdered precursors conditioned in an inert ceramic boat, which was gently placed in a quartz cylindrical tube. This setup was then placed in a tubular furnace which was equipped with temperature control and argon gas supply system. Initially, the pre-synthesized complex material is placed in a ceramic boat and purged with argon for 1.0 h in a quartz tube, before the commencement of heat treatment process. During the metal impregnation/complexation step, the metal precursor is dissolved in 50 mL of ethanol acting as solvent, with continuous stirring. When metal precursor dissolution is accomplished, then, the desired quantity of the ligand was added, while subjecting to continuous stirring using magnetic stirrer, and the mixture is refluxed for 1.0 h at the temperature range of 70 to 80 °C. During the refluxing step, the mixture altered its color from yellow (likely due to dissolved $\text{Fe}(\text{NO}_3)_3 \cdot 9\text{H}_2\text{O}$ in solution) to deep red, indicating the tris (1,10-phenanthroline) iron (II) complex formation, $[\text{Fe}(\text{Phen})_3]^{2+}$. After heating and stirring for 1.0 h, the carbon precursor was added, keeping stirring uninterrupted, and the mixture was refluxed under appropriate thermal control maintained between 60 and 70 °C for 5.0 h. After this interval, the iron-phenanthroline complex solution is left overnight at ambient condition for drying. After solvent evaporation, the complex is dried in an oven at 60 °C for 14 h. After drying, the synthesized complex was subjected pyrolysis at elevated temperatures of 500, 700, 1050, 1200, or 1300 °C, depending on the experiment, for 1.0 h, at the ramp rate of 1 °C min⁻¹, in a controlled atmosphere of argon, to yield the single-atom iron-based electrocatalyst. All synthesized electrocatalysts were formed by 1.0 wt.% Fe, and, herein, named as Fe-N-C, followed by the type of nitrogen source, in this case, Phen, (or Imi in some cases, depending on the experiment) and the carbon powder precursor, BP (or VC in some other few cases). The amounts of each precursor component for the syntheses are summarized in Table S1. For comparison, the different carbon supports were also subjected to pyrolysis at 1050 °C under Ar atmosphere, and their polarization curves were included in the ORR figures, along with that of the labeled Pt/C, referring to the state-of-the-art commercial PGM catalyst (20 wt.% Pt on Vulcan Carbon; E-TEK).

3.2. Physical Characterization

The crystalline structures of the metallic species were determined by XRD (ULTIMA IV, RIGAKU, Tokyo, Japan), with Cu K α radiation source. The diffractograms were obtained at room temperature and in the reflection mode, with a scan rate of 1.0° min^{−1} and step size of 0.02 by second. The samples were analyzed using the standard crystal data sheets of the EVA program (Brucker, Billerica, MA, USA). The specific surface areas of the electrocatalysts were determined via multilayer adsorption, using the BET isotherm method of N₂ adsorption (AutoChem II 2920, Micromeritics, Norcross, GA, USA). The electrocatalyst powder's metal content was measured by digesting samples in aqua regia using a microwave system, diluting to 50 mL, and analyzing with ICP-MS (PerkinElmer NexION 2000c, Waltham, MA, USA) against Fe-54 and Fe-56 standards from Carl Roth GmbH & Co. (Karlsruhe, Germany). HR-TEM measurements were conducted using a FEI (Hillsboro, OR, USA) Talos microscope, operated at 200 keV acceleration voltage, equipped with a Cold Field Emission Gun (FEG). STEM, with elemental mapping measurements were performed using a JEOL (Peabody, MA, USA) JEM-F200 microscopy, operated at 200 kV, equipped with FEG, and a 100 mm² silicon detector with drift correction and an EDS detector. XPS measurements were conducted in a ScientaOmicron (ESCA+ model, Uppsala, Sweden) equipment, equipped with a high-performance hemispheric analyzer (EAC 2000) with monochromatic Al K α ($h\nu$ = 1486.6 eV) anode operated at 12.5 kV. A pass energy of 50 eV with a 0.05 eV per step was used to record the high-resolution spectra. XAS spectra were obtained in the EXAFS region to investigate the structural characteristics of metal atoms with the carbon and nitrogen matrix. The spectra were obtained at Fe (7112 eV) K edge, and the measurements were carried out on the XAFS-2 beamline, at the Brazilian Synchrotron Light Laboratory (LNLS). The EXAFS oscillations signals were analyzed using Athena software (version 0.9.26) and were adjusted in the R space using K³ weight for the Fourier Transform.

3.3. Electrochemical Measurements

The electrocatalyst inks for the working electrodes were prepared in ethanol, with 5.0 mg of the electrocatalyst powder in 200 μ L of the solvent, with 50 μ L of Nafion[®] (5.0 wt.%). The prepared ink deposited on the top of a previously polished glassy carbon (GC) rotating disk electrode (RDE, 0.196 cm^{−2}, Pine Inst., Grove City, PA, USA), executing a drop-cast method, using a micro-pipette, and then, was allowed to dry to result in an electrocatalyst loading of 0.6 mg cm^{−2}. All electrochemical experiments were performed using an AUTOLAB potentiostat (Herisau, Switzerland, PGSTAT-30). The ORR activity was investigated in O₂-saturated 0.5 mol L^{−1} H₂SO₄ electrolyte, in a glass cell equipped with typical three electrode assembly. The reference electrode was a leak-free KCl-saturated Ag/AgCl/Cl[−], but all potentials were quoted versus the Reversible Hydrogen Reference (RHE) electrode. The counter electrode was a graphite rod. In all trails of experiments, the electrolyte was saturated by purging the desired gas, which may be either argon or oxygen, depending on the experiment, for 20 min. Cyclic voltammetry was conducted at 50 mV s^{−1} until stable current profile. The ORR was studied via linear sweep voltammetry (LSV), at 1.0 mV s^{−1}, at 1600 rpm. Accelerated stability tests were conducted via potential stair-step from 0.40 to 0.7 V vs. Ag/AgCl, with a total of 10.000 steps. The activity and stability of the best performing Fe-N-C electrocatalyst was evaluated using Membrane Electrode Assemblies (MEAs) of a PEM fuel cell. The cathode catalyst ink (35.5 wt.% Nafion ionomer) was prepared by ultrasonically mixing Fe-N-C, deionized water, isopropanol, and a 5.0 wt.% Nafion suspension. A commercial 20 wt.% Pt/C (E-Tek) electrocatalyst served as the anode, with ink (35.5 wt.% Nafion ionomer) prepared under similar conditions. Inks were applied to the microporous side of a carbon cloth (4.0 cm²) and dried under vacuum

at 60 °C for 2 h. The MEA was assembled by hot-pressing a Nafion (Wilmington, DE, USA) 115 membrane between the electrodes at 120 °C and 5 MPa for 1.0 min.

4. Conclusions

Fe-N-C electrocatalysts were optimized by adjusting fundamental parameters of the phenanthroline-iron complexation method, including Fe/Phen atomic ratio, carbon support surface area, and pyrolysis temperature, to improve ORR performance and durability. The results demonstrated that electrocatalysts synthesized using 1,10-phenanthroline and high-surface-area Black Pearls carbon exhibited significantly superior ORR performance compared to those prepared with Vulcan carbon. Structural characterizations by EXAFS and XRD revealed that these less active materials predominantly contained inactive features, such as encapsulated iron nanoparticles. These findings highlight the synergistic role of the bidentate ligand and the high-surface-area carbon in promoting atomic dispersion of iron and the formation of highly active Fe-N-C single-atom sites after pyrolysis. Additionally, a distinct improvement in electrocatalyst stability was observed during accelerated durability tests and air storage as the pyrolysis temperature increased from 700 °C to 1300 °C. However, this thermal treatment led to a considerable decline in ORR activity, likely due to the formation of iron particles. The electrocatalysts synthesized at 1050 °C yielded the electrocatalyst with the most favorable balance of activity and stability in half-cell measurements while maintaining moderate durability under PEM fuel cell operation. The material prepared at 1200 °C, although with inferior ORR activity, appears to be a promising candidate for future optimization strategies aimed at improving electrocatalytic activity without compromising its inherent stability. Overall, the insights gained from this study may guide the development of highly active and durable electrocatalysts, produced via a simple and scalable method using earth-abundant elements, for use in PEM fuel cell cathodes.

Supplementary Materials: The following supporting information can be downloaded at <https://www.mdpi.com/article/10.3390/catal15090821/s1>. Table S1: Nominal weight percentages of components in the different synthesized electrocatalyst, varying iron, nitrogen, and carbon sources; Table S2: BET surface areas of the powders synthesized using different N-containing molecules and carbon sources; Figure S1: TEM images obtained for the Fe-N-C electrocatalyst synthesized using 1,10-phenanthroline and Black Pearls with different iron-to-nitrogen ratios; Figure S2: X-ray powder diffraction of the Fe-N-C electrocatalysts synthesized using 1,10-phenanthroline and Black Pearls carbon, with different loadings of iron; Figure S3: X-ray powder diffraction for the Fe-N-C electrocatalysts synthesized using phenanthroline (red) or imidazole (black); Figure S4: STEM images and the corresponding elemental mapping, as indicated in the figure inset, for the Fe-N-C electrocatalysts synthesized using 1,10-phenanthroline and Black Pearls (Fe-N-C Phen BP; (left)) or Vulcan carbon (Fe-N-C Phen VC; (right)); Figure S5: (A) HR-TEM (a), STEM (b) images and the corresponding elemental mapping for iron and oxygen (c and d) obtained for the Fe-N-C electrocatalyst synthesized using 1,10-phenanthroline and Vulcan carbon (Fe-N-C Phen VC 1050), and (B) HR-TEM and the corresponding elemental mapping of iron (top) and oxygen (bottom) of an individual iron-oxide nanoparticle; Figure S6: Deconvolution of the XPS spectra for the Fe 2p and nitrogen N 1s of the Fe-N-C Phen BP electrocatalyst; Figure S7: Linear sweep voltammetry (LSV) curves for the oxygen reduction on Fe-N-C Phen BP 1050 electrocatalysts synthesized with 5.0 and 10.0 wt.% Fe, obtained in O₂-saturated 0.5 mol L⁻¹ H₂SO₄ electrolyte, with scan rate of 1.0 mV s⁻¹ and rotation rate of 1600 rpm; Figure S8: Linear sweep voltammetry (LSV) curves for the oxygen reduction on Fe-N-C synthesized using imidazole (instead of Phen) and BP carbon, obtained in O₂-saturated 0.5 mol L⁻¹ H₂SO₄ electrolyte, with scan rate of 1.0 mV s⁻¹ and rotation rate of 1600 rpm; Figure S9: Cyclic voltammetry (CV) curves for Fe-N-C Phen BP (red) and Fe-N-C Phen VC (blue), obtained in Ar-saturated 0.5 mol L⁻¹ H₂SO₄ electrolyte, with scan rate of 50 mV s⁻¹;

Figure S10: Linear sweep voltammetry (LSV) curves for the oxygen reduction on Fe-N-C Phen VC before (thin red line) and after treatment in NH_3 , at $900\text{ }^\circ\text{C}$ (thick red line), obtained in O_2 -saturated $0.5\text{ mol L}^{-1}\text{ H}_2\text{SO}_4$ electrolyte, with scan rate of 1.0 mV s^{-1} and rotation rate of 1600 rpm (the curves for the ORR on pure Vulcan carbon and Pt/C were included for comparison); Figure S11: Fourier Transform of the EXAFS oscillations, K^3 -weighted, at the Fe (7112 eV) K edge, for the Fe-N-C Phen VC electrocatalyst further step of treatment in NH_3 at $900\text{ }^\circ\text{C}$. The reference spectrum for Fe foil was included for comparison; Figure S12: Deconvoluted Raman spectra of Fe-N-C Phen BP electrocatalysts prepared at different pyrolysis temperatures. The band assignments are provided in the figure inset legend; Figure S13: LSV curves recorded before and after the Fe-N-C Phen BP electrocatalyst storage (shelf-life), for different periods of time, as indicated in the figure inset legend, synthesized at pyrolysis temperatures of $700\text{ }^\circ\text{C}$ (a) $1050\text{ }^\circ\text{C}$ (b), obtained in O_2 -saturated $0.5\text{ mol L}^{-1}\text{ H}_2\text{SO}_4$ electrolyte, with scan rate of 1.0 mV s^{-1} and rotation rate of 1600 rpm.

Author Contributions: Conceptualization, F.H.B.L., C.S.A.V. and N.A.G.; methodology, C.S.A.V., N.K. and E.A.P.-S.; formal analysis, F.H.B.L. and K.S.; investigation, C.S.A.V., M.L.S. and M.L.; resources, F.H.B.L.; data curation, F.H.B.L.; writing—original draft preparation, C.S.A.V.; writing—review and editing, F.H.B.L. and N.K.; project administration, F.H.B.L.; funding acquisition, F.H.B.L. All authors have read and agreed to the published version of the manuscript.

Funding: Authors gratefully acknowledge financial support from FAPESP (São Paulo Research Foundation); F.H.B.L. (Thematic project; grant # 2019/22183-6). F.H.B.L. and C.S.A.V. also acknowledge financial support from CNPq (Conselho Nacional de Desenvolvimento Científico e Tecnológico) (grant # 308948/2022-0, 406933/2021-9, 134577/2018-3, and 140893/2021-0).

Data Availability Statement: Data are contained within the article and Supplementary Materials.

Acknowledgments: Authors also acknowledge Richard F. Webster, Richard Tilley, and the facilities and scientific and technical assistance of Microscopy Australia at the Electron Microscope Unit (EMU) within the Mark Wainwright Analytical Centre (MWAC) at UNSW Sydney. This work was also in part supported by the Million Mile Fuel Cell Truck (M2FCT) Consortium, technology manager Greg Kleen, the U.S. DOE, Office of Energy Efficiency and Renewable Energy, Hydrogen and Fuel Cell Technologies Office, under contract no. DE-SC0012704. This research used Electron Microscopy resources of the Center for Functional Nanomaterials (CFN), which is a U.S. Department of Energy Office of Science User Facility, at Brookhaven National Laboratory under contract no. DE-SC0012704, and the Electron Microscopy resources of the Laboratório Nacional de Nanotecnologia (LNNano) at Centro Nacional de Pesquisa em Energia e Materiais (CNPEM).

Conflicts of Interest: The authors declare no conflict of interest.

References

1. Dubau, L.; Castanheira, L.; Maillard, F.; Chatenet, M.; Lottin, O.; Maranzana, G.; Dillet, J.; Lamibrac, A.; Perrin, J.C.; Moukheiber, E.; et al. A Review of PEM Fuel Cell Durability: Materials Degradation, Local Heterogeneities of Aging and Possible Mitigation Strategies. *Wiley Interdiscip. Rev. Energy Environ.* **2014**, *3*, 540–560. [[CrossRef](#)]
2. Lopes, P.P.; Li, D.; Lv, H.; Wang, C.; Tripkovic, D.; Zhu, Y.; Schimmenti, R.; Daimon, H.; Kang, Y.; Snyder, J.; et al. Eliminating Dissolution of Platinum-Based Electrocatalysts at the Atomic Scale. *Nat. Mater.* **2020**, *19*, 1207–1214. [[CrossRef](#)] [[PubMed](#)]
3. Gong, M.; Mehmood, A.; Ali, B.; Nam, K.W.; Kucernak, A. Oxygen Reduction Reaction Activity in Non-Precious Single-Atom (M-N/C) Catalysts—Contribution of Metal and Carbon/Nitrogen Framework-Based Sites. *ACS Catal.* **2023**, *13*, 6661–6674. [[CrossRef](#)]
4. He, Y.; Guo, H.; Hwang, S.; Yang, X.; He, Z.; Braaten, J.; Karakalos, S.; Shan, W.; Wang, M.; Zhou, H.; et al. Single Cobalt Sites Dispersed in Hierarchically Porous Nanofiber Networks for Durable and High-Power PGM-Free Cathodes in Fuel Cells. *Adv. Mater.* **2020**, *32*, 2003577. [[CrossRef](#)]
5. Banham, D.; Kishimoto, T.; Zhou, Y.; Sato, T.; Bai, K.; Ozaki, J.I.; Imashiro, Y.; Ye, S. Critical Advancements in Achieving High Power and Stable Nonprecious Metal Catalyst-Based MEAs for Real-World Proton Exchange Membrane Fuel Cell Applications. *Sci. Adv.* **2018**, *4*, eaar7180. [[CrossRef](#)]

6. Kumar, K.; Gairola, P.; Lions, M.; Ranjbar-Sahraie, N.; Mermoux, M.; Dubau, L.; Zitolo, A.; Jaouen, F.; Maillard, F. Physical and Chemical Considerations for Improving Catalytic Activity and Stability of Non-Precious-Metal Oxygen Reduction Reaction Catalysts. *ACS Catal.* **2018**, *8*, 11264–11276. [\[CrossRef\]](#)
7. Ahluwalia, R.K.; Wang, X.; Osmieri, L.; Peng, J.-K.; Cetinbas, C.F.; Park, J.; Myers, D.J.; Chung, H.T.; Neyerlin, K.C. Stability of Atomically Dispersed Fe-N-C ORR Catalyst in Polymer Electrolyte Fuel Cell Environment. *J. Electrochem. Soc.* **2021**, *168*, 024513. [\[CrossRef\]](#)
8. Cui, P.; Zhao, L.; Long, Y.; Dai, L.; Hu, C. Carbon-Based Electrocatalysts for Acidic Oxygen Reduction Reaction. *Angew. Chem. Int. Ed.* **2023**, *62*, e202218269. [\[CrossRef\]](#)
9. Zhao, Y.; Yin, P.; Yang, Y.; Wang, R.; Gong, C.; Li, J.; Guo, J.; Wang, Q.; Ling, T. Converting Fe-N-C Single-atom Catalyst to a New Fe_NxSe_y Cluster Catalyst for Proton-exchange Membrane Fuel Cells. *Angew. Chem. Int. Ed.* **2025**, *64*, e202419501. [\[CrossRef\]](#)
10. Ramaswamy, N.; Mukerjee, S. Influence of Inner- and Outer-Sphere Electron Transfer Mechanisms During Electrocatalysis of Oxygen Reduction in Alkaline Media. *J. Phys. Chem. C* **2011**, *115*, 18015–18026. [\[CrossRef\]](#)
11. Yang, N.; Peng, L.; Li, L.; Li, J.; Liao, Q.; Shao, M.; Wei, Z. Theoretically Probing the Possible Degradation Mechanisms of an FeNC Catalyst During the Oxygen Reduction Reaction. *Chem. Sci.* **2021**, *12*, 12476–12484. [\[CrossRef\]](#) [\[PubMed\]](#)
12. Chenitz, R.; Kramm, U.I.; Lefèvre, M.; Glibin, V.; Zhang, G.; Sun, S.; Dodelet, J.P. A Specific Demetalation of Fe-N₄ Catalytic Sites in the Micropores of NC_Ar + NH₃ is at the Origin of the Initial Activity Loss of the Highly Active Fe/N/C Catalyst Used for the Reduction of Oxygen in PEM Fuel Cells. *Energy Environ. Sci.* **2018**, *11*, 365–382. [\[CrossRef\]](#)
13. Rauf, M.; Di Zhao, Y.; Wang, Y.C.; Zheng, Y.P.; Chen, C.; Yang, X.D.; Zhou, Z.Y.; Sun, S.G. Insight into the Different ORR Catalytic Activity of Fe/N/C Between Acidic and Alkaline Media: Protonation of Pyridinic Nitrogen. *Electrochem. Commun.* **2016**, *73*, 71–74. [\[CrossRef\]](#)
14. Choi, C.H.; Lim, H.-K.; Chon, G.; Chung, M.W.; Altin, A.; Sahraie, N.R.; Sougrati, M.-T.; Stievano, L.; Oh, H.S.; Park, E.S.; et al. The Achilles' Heel of Iron-Based Catalysts During Oxygen Reduction in an Acidic Medium. *Energy Environ. Sci.* **2018**, *11*, 3176–3182. [\[CrossRef\]](#)
15. Bai, J.; Zhao, T.; Xu, M.; Mei, B.; Yang, L.; Shi, Z.; Zhu, S.; Wang, Y.; Jiang, Z.; Zhao, J.; et al. Monosymmetric Fe-N₄ Sites Enabling Durable Proton Exchange Membrane Fuel Cell Cathode by Chemical Vapor Modification. *Nat. Commun.* **2024**, *15*, 4219. [\[CrossRef\]](#)
16. Na, G.; Hwang, W.; Shin, H.; Park, S.; Park, J.E.; Lee, J.; Shin, Y.; Choi, H.; Shim, J.; Yeom, K.; et al. Durable and Active Nitrogen-Coordinated Iron Single-Atom Catalyst for Proton Exchange Membrane Fuel Cells Through Carbon Encapsulation. *Adv. Energy Mater.* **2024**, *14*, 2400565. [\[CrossRef\]](#)
17. Zhang, L.; Dong, Y.; Li, L.; Shi, Y.; Zhang, Y.; Wei, L.; Dong, C.L.; Lin, Z.; Su, J. Concurrently Boosting Activity and Stability of Oxygen Reduction Reaction Catalysts via Judiciously Crafting Fe-Mn Dual Atoms for Fuel Cells. *Nanomicro Lett.* **2025**, *17*, 88. [\[CrossRef\]](#)
18. Ye, W.; Chen, S.; Lin, Y.; Yang, L.; Chen, S.; Zheng, X.; Qi, Z.; Wang, C.; Long, R.; Chen, M.; et al. Precisely Tuning the Number of Fe Atoms in Clusters on N-Doped Carbon Toward Acidic Oxygen Reduction Reaction. *Chem* **2019**, *5*, 2865–2878. [\[CrossRef\]](#)
19. He, Y.; Liu, S.; Priest, C.; Shi, Q.; Wu, G. Atomically Dispersed Metal–Nitrogen–Carbon Catalysts for Fuel Cells: Advances in Catalyst Design, Electrode Performance, and Durability Improvement. *Chem. Soc. Rev.* **2020**, *49*, 3484–3524. [\[CrossRef\]](#)
20. Sahraie, N.R.; Kramm, U.I.; Steinberg, J.; Zhang, Y.; Thomas, A.; Reier, T.; Paraknowitsch, J.P.; Strasser, P. Quantifying the Density and Utilization of Active Sites in Non-Precious Metal Oxygen Electroreduction Catalysts. *Nat. Commun.* **2015**, *6*, 8618. [\[CrossRef\]](#)
21. Yang, H.; Shang, L.; Zhang, Q.; Shi, R.; Waterhouse, G.I.N.; Gu, L.; Zhang, T. A Universal Ligand Mediated Method for Large Scale Synthesis of Transition Metal Single Atom Catalysts. *Nat. Commun.* **2019**, *10*, 4585. [\[CrossRef\]](#) [\[PubMed\]](#)
22. Kim, M.; Yoo, J.M.; Ahn, C.-Y.; Jang, J.-H.; Son, Y.J.; Shin, H.; Kang, J.; Kang, Y.S.; Yoo, S.J.; Lee, K.-S.; et al. Rational Generation of Fe-N_x Active Sites in Fe-N-C Electrocatalysts Facilitated by Fe-N Coordinated Precursors for the Oxygen Reduction Reaction. *ChemCatChem* **2019**, *11*, 5982–5988. [\[CrossRef\]](#)
23. Woo, J.; Yang, S.Y.; Sa, Y.J.; Choi, W.Y.; Lee, M.H.; Lee, H.W.; Shin, T.J.; Kim, T.Y.; Joo, S.H. Promoting Oxygen Reduction Reaction Activity of Fe-N/C Electrocatalysts by Silica-Coating-Mediated Synthesis for Anion-Exchange Membrane Fuel Cells. *Chem. Mater.* **2018**, *30*, 6684–6701. [\[CrossRef\]](#)
24. Li, X.; Li, P.; Yang, J.; Xie, L.; Wang, N.; Lei, H.; Zhang, C.; Zhang, W.; Lee, Y.M.; Zhang, W.; et al. A Cobalt (II) Porphyrin with a Tethered Imidazole for Efficient Oxygen Reduction and Evolution Electrocatalysis. *J. Energy Chem.* **2023**, *76*, 617–621. [\[CrossRef\]](#)
25. Snitkoff, R.Z.; Levy, N.; Ozery, I.; Ruthstein, S.; Elbaz, L. Imidazole Decorated Reduced Graphene Oxide: A Biomimetic Ligand for Selective Oxygen Reduction Electrocatalysis with Metalloporphyrins. *Carbon* **2019**, *143*, 223–229. [\[CrossRef\]](#)
26. Du, C.; Gao, Y.; Chen, H.; Li, P.; Zhu, S.; Wang, J.; He, Q.; Chen, W. A Cu and Fe Dual-Atom Nanozyme Mimicking Cytochrome C Oxidase to Boost the Oxygen Reduction Reaction. *J. Mater. Chem. A* **2020**, *8*, 16994–17001. [\[CrossRef\]](#)
27. Mamtani, K.; Singh, D.; Tian, J.; Millet, J.M.M.; Miller, J.T.; Co, A.C.; Ozkan, U.S. Evolution of N-Coordinated Iron-Carbon (FeNC) Catalysts and their Oxygen Reduction (ORR) Performance in Acidic Media at Various Stages of Catalyst Synthesis: An Attempt at Benchmarking. *Catal. Lett.* **2016**, *146*, 1749–1770. [\[CrossRef\]](#)

28. Yin, S.; Yi, H.; Liu, M.; Yang, J.; Yang, S.; Zhang, B.W.; Chen, L.; Cheng, X.; Huang, H.; Huang, R.; et al. An *In Situ* Exploration of How Fe/N/C Oxygen Reduction Catalysts Evolve During Synthesis under Pyrolytic Conditions. *Nat. Commun.* **2024**, *15*, 6229. [[CrossRef](#)]
29. Guan, D.; Xu, H.; Huang, Y.-C.; Jing, C.; Tsujimoto, Y.; Xu, X.; Lin, Z.; Tang, J.; Wang, Z.; Sun, X.; et al. *Operando* Studies Redirect Spatiotemporal Restructuration of Model Coordinated Oxides in Electrochemical Oxidation. *Adv. Mater.* **2025**, *37*, 2413073. [[CrossRef](#)]
30. Qian, Z.; Hu, Z.; Zhang, Z.; Li, Z.; Dou, M.; Wang, F. Out-of-Plane FeII-N₄ Moiety Modified Fe-N Co-Doped Porous Carbons as High-Performance Electrocatalysts for the Oxygen Reduction Reaction. *Catal. Sci. Technol.* **2017**, *7*, 4017–4023. [[CrossRef](#)]
31. Zou, D.; Yi, Y.; Song, Y.; Guan, D.; Xu, M.; Ran, R.; Wang, W.; Zhou, W.; Shao, Z. The BaCe_{0.16}Y_{0.04}Fe_{0.80}O_{3-δ} Nanocomposite: A New High-Performance Cobalt-Free Triple-Conducting Cathode for Protonic Ceramic Fuel Cells Operating at Reduced Temperatures. *J. Mater. Chem. A* **2022**, *10*, 5381. [[CrossRef](#)]
32. Xia, D.; Tang, X.; Dai, S.; Ge, R.; Rykov, A.; Wang, J.; Huang, T.-H.; Wang, K.-W.; Wei, Y.; Zhang, K.; et al. Ultrastable Fe-N-C Fuel Cell Electrocatalysts by Eliminating Non-Coordinating Nitrogen and Regulating Coordination Structures at High Temperatures. *Adv. Mater.* **2023**, *35*, 2204474. [[CrossRef](#)] [[PubMed](#)]
33. Teixeira Santos, K.; Kumar, K.; Dubau, L.; Ge, H.; Berthon-Fabry, S.; Vasconcellos, C.S.A.; Lima, F.H.B.; Asset, T.; Atanassov, P.; Saveleva, V.A.; et al. Spontaneous Aerobic Ageing of Fe-N-C Materials and Consequences on Oxygen Reduction Reaction Kinetics. *J. Power Sources* **2023**, *564*, 232829. [[CrossRef](#)]
34. Guo, W.; Pan, M.; Xie, Q.; Fan, H.; Luo, L.; Jing, Q.; Shen, Y.; Yan, Y.; Liu, M.; Wang, Z. Achieving pH-Universal Oxygen Electrolysis via Synergistic Density and Coordination Tuning Over Biomass-Derived Fe Single-Atom Catalyst. *Nat. Commun.* **2025**, *16*, 2920. [[CrossRef](#)]

Disclaimer/Publisher’s Note: The statements, opinions and data contained in all publications are solely those of the individual author(s) and contributor(s) and not of MDPI and/or the editor(s). MDPI and/or the editor(s) disclaim responsibility for any injury to people or property resulting from any ideas, methods, instructions or products referred to in the content.